




Received March 20, 2024; accepted May 28, 2024; Date of publication June 18, 2024. 
The review of this paper was arranged by Associate Editor Montê A. Vitorino  and Editor-in-Chief Heverton A. Pereira 

Digital Object Identifier <http://doi.org/10.18618/REP.2005.1.029036>

Generalized Average Model of the Class-E² DC-DC Resonant converter

Lucas S. Mendonça ¹, Fábio E. Bisogno ²

¹Federal University of Technology – Paraná, Academic Department of Electronics, Curitiba, PR, Brazil.

²Hochschule Koblenz, Lehrgebiet Elektronik, Koblenz, Germany.

e-mail: lucasmendonca@utfpr.edu.br; fbisogno@gmail.com

ABSTRACT In this paper, the generalized average model of the Class-E² DC-DC resonant converter has been introduced. The standard average model is not interesting in resonant converters due to their large waveform oscillations. In addition, steady-state approaches restrain the converter to hysteresis control. The resonant tank voltage, reconstructed by the fundamental component, as performed in LLC converters by extended describing function, is not suitable for the Class-E² topology because the inverter/rectifier interface voltage requires, at least, the third-order harmonic usage. This work relies on the generalized average method to perform the large-signal and small-signal models of the Class-E² converter. This paper shows how to systematically deal with the following modeling issues: negative index from the convolution summation, complex numbers from the Fourier coefficients and high number of state-space variables. The theoretical approach is confirmed by measurement in an assembled 800 kHz Class-E² converter based on voltage-controlled oscillator.

KEYWORDS Circuit modeling, dc-dc power converters¹, resonant converters.

I. INTRODUCTION

Power electronic converters can be divided in hard-switching/pulse-width modulation (PWM) converters and soft-switching/resonant converters. Considering high frequency operation, which leads to small hardware size and high-power density, Class-E DC-DC based topologies are the cutting-edge technologies due to their double soft-switching feature (both inverter switch and rectifier diode) [1], [2]. However, a well-designed resonant converter requires the steady-state and dynamic analysis, which have new challenges introduced by the specificities of each application.

The steady-state analysis provides a way to design the converter considering a nominal operating point, which allows to select the hardware components. On the other side, the dynamic analysis is used to verify how disturbances affect the circuit variables. For hard-switching converters, the averaged model, which can be performed by circuit or state-space models [3], is commonly used. This technique is not suitable in resonant converters due to their large ripple waveforms and high harmonic content.

The averaged model application is well-known for Buck, Boost and Buck-Boost DC-DC converters [4], [3]. It can also be applied in fourth-order converters, like as Ćuk [4], Sepic [5] and Zeta [6], [7]. The authors in [8], have proposed a reduced-order average circuit for the dual-active-bridge converter (DAB) in which, the primary side current (produced by the full-bridge inverter) and the secondary side current (input for the full-bridge rectifier) are represented as independent current sources. Although the circuit can be easily simulated, it is worth to mention that the converter does

not use a resonant tank, which simplifies the mathematical development.

The small ripple approximation used in the traditional averaged model can not be applied in resonant converters because their circuit variables do not have small oscillations like the basic aforementioned DC-DC converters. In addition, if the perturbation frequency is near to the half of the switching frequency, the sideband effect is non-negligible, thus, the averaged model is inaccurate [9].

Envisaging the output power control of DC-DC resonant converters based on Class-E topologies, literature shows main techniques as pulse frequency modulation (PFM) [10], pulse-width modulation (PWM) [11], ON-OFF control [12] and dual-frequency control [13]. Usually, instead of developing a small-signal model, these techniques rely on a comprehensive steady-state formulation that maps the operational regions of the converter. PFM uses different frequencies to change the converter operating point while PWM relies on the modification of the power switch gate signal pulse-width. Both approaches lead to sub-optimum operation (i.e., soft-switching capabilities are loss). By means of a low-frequency dimming for the output power, the ON-OFF control works by changing the converter between two states: nominal average power (ON-state) and zero power (OFF-state). The main drawback of the ON-OFF control is the large output voltage ripple due to increased transition time. In this regard, the dual-frequency control is able to reduce the transition time by setting a range for the power that does not reach zero. As an example, in [13], a Class-E Boost converter with dual-frequency control was designed to achieve zero transient time while keeping the soft-switching for both selected

frequencies of 4 MHz (high-power state) and 8 MHz (low-power state). In [14], a Class-ED converter was designed to operate with multiple frequencies that deal with multiple input power levels and it can be considered as a hysteresis control that reduces the mode transition losses. For the sake of nomenclature, this paper considers the PFM, PWM, ON-OFF and dual-frequency control as steady-state modeling approaches that are used as background for the control design of DC-DC converters. These steady-state techniques restrain the converter to hysteresis control.

Aiming to deal with the downsides of the aforementioned methods, the generalized average method (GAM) can be applied to represent the large and small-signal models of power converters. The GAM captures different harmonic components and the reconstruction of the waveforms is based on the Fourier series. In [15], the Buck, Boost and Buck-Boost converters were analyzed by GAM. It also describes the operation at any number of operating phases with switching dynamics of phases. A small-signal model for the Class-E cascaded to a full-bridge rectifier (Class-E FB) with a LC output filter was performed in [16]. A Class-E inverter drives a piezoelectric transformer and then, a full-bridge rectifier adapts the secondary voltage to supply a DC load.

It is worth to mention the extended describing function (EDF) as a small-signal modeling technique. This method was introduced in [17] and it is derived from the GAM. Although some steps in EDF and GAM are interchangeable, the EDF application has been reported limiting the harmonics to: the fundamental sine and cosine in LLC resonant converter [18] and third-order harmonics for Class-ED converter [17]. However, in the reported Class-ED application, the third-order harmonic was only used for the inverter switch voltage. In contrast, in the Class-E² converter, it is also necessary to use high-order harmonics for the rectifier diode voltage.

Even though the GAM is addressed in several topologies, it was not solved for the Class-E² converter because obstacles arise due to the complexity of this topology regarding number of components and harmonic content. The GAM requires a trade-off between accuracy and complexity which is determined by the selected number of harmonics. For second order converters, it is possible to achieve reasonable accuracy by using the DC component and first-order harmonic. Considering DAB and LLC converters, the inverter switches and resonant tank can be modeled by the fundamental component. Moreover, Class-E inverter cascaded with Class-D or full-bridge rectifier can be dealt by simplifying the output subsystem as a constant DC source. The aforementioned dynamic model techniques for DC-DC converters are summarized in Table 1.

The preceding assumptions can not be used in the Class-E² model. Therefore, the following statements outline the problem addressed in this work:

- 1) The single inverter switch and rectifier diode connected to parallel capacitors in the Class-E² topology generate

high harmonic content waveforms which can not be described by standard sources. Thus, the representation considering the fundamental sine and cosine in EDF as shown in [26] can not be used to model the resonant tank of the Class-E² like in DAB and LLC converters;

- 2) To achieve reasonable accuracy, the complexity of the model can not be reduce as shown in [15]. It is because, at least three harmonics must be considered to model the Class-E² converter;
- 3) The Class-E² converter has 7 reactive components, which leads to a highly complex model. It is going to be shown that the number of state variables is: the order of the system plus $2 \times$ number of harmonics \times order of the system; leading to at least 49 state variables by considering the third-order harmonics. Thus, it requires an automatic model construction algorithm to represent and solve the set of differential equations;
- 4) Application of EDF considering high order harmonics was reported for the Class-ED converter in [17], in which, the harmonics were truncated on the third-order component for the inverter switch. However, the rectifier input voltage was reconstructed only by the fundamental component. In contrast, the Class-E² converter requires the third-order harmonic usage in the rectifier input voltage (diode voltage).

In this paper, the generalized average model of the Class-E² DC-DC resonant converter is introduced. The theoretical approach is validated by an assembled 800 kHz Class-E² converter.

II. CLASS-E² DC-DC RESONANT CONVERTER

The Class-E² resonant converter in Figure 1 is composed of: input voltage V_{in} , choke inductor L_c , switch S , inverter capacitor C_1 , resonant inductor L_r , resonant capacitor C_r , diode D , rectifier capacitor C_2 , output filter $L_f - C_f$ and a load R_L . The circuit variables are described as: currents i_{L_c} ,

Table 1. Dynamic Modeling Techniques in DC-DC Conversion

Converter	Averaged	EDF	Steady-State	GAM
Buck	[4]			[19]
Boost	[4], [20], [21]			[19], [22]
Buck-Boost	[4]			[19]
Ćuk	[4]			
Sepic	[5]			
Zeta	[6], [7]			
Quasi-resonant	[23]			
DAB	[8]			[24], [25]
LLC		[18], [26]		
Class-DE				[15]
Class-E Boost			[13]	
Class-E FB	[27]			[16]
Class-ED		[17]	[12], [14]	
Class-E ²			[28]	

i_S , i_{L_r} , i_D , i_{L_f} and I_o ; and voltages v_S , v_{C_1} , v_{C_r} , v_D , v_{C_2} , v_{C_f} and V_o [29]. The converter has four operating modes. In the end of each cycle, switch S turns-on with zero-voltage soft-switching (ZVS). The diode D turns off at the end of mode III with zero-derivative voltage soft-switching (ZDVS). The switch S is ruled by duty cycle D_c ; T_1 and T_2 indicate the end of modes I and III, respectively. By considering the state variables as i_{L_c} , v_{C_1} , i_{L_r} , v_{C_r} , v_{C_2} , i_{L_f} and v_{C_f} , the differential equations for each operating mode are described in Table 2. For all modes, $\frac{dv_{C_f}}{dt} = \frac{i_{L_f}}{C_f} - \frac{v_{C_f}}{R_L C_f}$.

The voltage v_{C_2} is the interface circuit variable between the inverter and rectifier sub-systems. It is the voltage provided by the resonant tank which is the input for the rectifier. This voltage has high harmonic content as shown in Figure 2 and, by anticipating the results, it is necessary to use, at least, the third-order harmonic to achieve a suitable waveform reconstruction. In contrast, the DAB and LLC converters can be modeled by the fundamental component [18], [26].

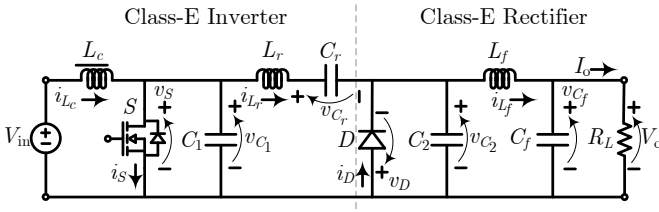


Figure 1. Class-E² DC-DC resonant converter.

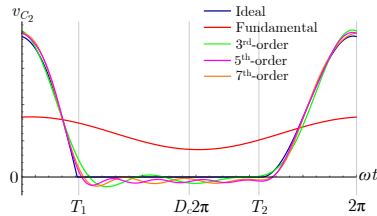


Figure 2. Rectifier input voltage (rectifier capacitor voltage, v_{C_2}).

Table 2. Differential Equations for the Class-E² Resonant Converter

Variable	Mode I	Mode II	Mode III	Mode IV
$\frac{di_{L_c}}{dt}$	$\frac{V_{in}}{L_c}$	$\frac{V_{in}}{L_c}$	$\frac{V_{in}-v_{C_1}}{L_c}$	$\frac{V_{in}-v_{C_1}}{L_c}$
$\frac{dv_{C_1}}{dt}$	0	0	$\frac{i_{L_c}-i_{L_r}}{C_1}$	$\frac{i_{L_c}-i_{L_r}}{C_1}$
$\frac{di_{L_r}}{dt}$	$\frac{-v_{C_r}-v_{C_2}}{L_r}$	$\frac{-v_{C_r}}{L_r}$	$\frac{v_{C_1}-v_{C_r}}{L_r}$	$\frac{v_{C_1}-v_{C_r}-v_{C_2}}{L_r}$
$\frac{dv_{C_r}}{dt}$	$\frac{i_{L_r}}{C_r}$	$\frac{i_{L_r}}{C_r}$	$\frac{i_{L_r}}{C_r}$	$\frac{i_{L_r}}{C_r}$
$\frac{dv_{C_2}}{dt}$	$\frac{i_{L_r}-i_{L_f}}{C_2}$	0	0	$\frac{i_{L_r}-i_{L_f}}{C_2}$
$\frac{di_{L_f}}{dt}$	$\frac{v_{C_2}-v_{C_f}}{L_f}$	$\frac{-v_{C_f}}{L_f}$	$\frac{-v_{C_f}}{L_f}$	$\frac{v_{C_2}-v_{C_f}}{L_f}$

III. SWITCHING FUNCTION

The Class-E² converter has four operating modes ruled by the switch S and the diode D operation. In this sense, two

switching functions should be defined, which generate state-space models for each mode. The switching functions are defined as Fourier series [30]:

$$f_{1,2}(t) = \langle s_{1,2} \rangle_0 + \sum_{k=1}^{k_{\max}} (\langle s_{1,2} \rangle_k e^{jkt} + \langle s_{1,2} \rangle_{-k} e^{-jkt}), \quad (1)$$

in which, $f_{1,2}(t)$ is the switching function, notation $\langle \rangle_k$ represents the function evaluated considering harmonic k , k_{\max} is the maximum number of considered harmonics and $\langle s_{1,2} \rangle_k$ represents the Fourier coefficient for harmonic k . Subscripts 1 and 2 are used to represent the effect of the switch S or the diode D , respectively.

The Fourier coefficients are calculated by considering the integration intervals with respect to the switch and diode operations:

$$\langle s_1 \rangle_k = \frac{1}{2\pi} \left(\int_{D_c 2\pi}^{2\pi} e^{-jk\tau} d\tau \right) \quad (2)$$

and

$$\langle s_2 \rangle_k = \frac{1}{2\pi} \left(\int_0^{T_1} e^{-jk\tau} d\tau + \int_{T_2}^{2\pi} e^{-jk\tau} d\tau \right). \quad (3)$$

Switching function $f_1(t)$ is able to represent the transitions on-off and off-on for the switch S . In the same way, switching function $f_2(t)$ represents the transitions off-on and on-off for the diode D .

In this sense, non-linear differential equations can be used to represent the Class-E² in a single set of equations based on the linear differential equations shown in Table 2 and the switching functions $f_1(t)$ and $f_2(t)$. In (2), the coefficients of $f_1(t)$ are defined at the interval $D_c 2\pi - 2\pi$. This means that, by multiplying the terms in the differential equations by $f_1(t)$, the terms are turned into zero at modes I and II. In the same way, by multiplying the terms in the differential equations by $f_2(t)$, the terms are turned into zero at modes II and III due to the limits in the integral calculation in (3). Based on that, the non-linear equations are described as:

$$\frac{di_{L_c}(t)}{dt} = \frac{V_{in}}{L_c} - \frac{v_{C_1}(t)}{L_c} f_1(t), \quad (4)$$

$$\frac{dv_{C_1}(t)}{dt} = \frac{i_{L_c}(t)}{C_1} f_1(t) - \frac{i_{L_r}(t)}{C_1} f_1(t), \quad (5)$$

$$\frac{di_{L_r}(t)}{dt} = \frac{v_{C_1}(t)}{L_r} f_1(t) - \frac{v_{C_r}(t)}{L_r} - \frac{v_{C_2}(t)}{L_r} f_2(t), \quad (6)$$

$$\frac{dv_{C_r}(t)}{dt} = \frac{i_{L_r}(t)}{C_r}, \quad (7)$$

$$\frac{dv_{C_2}(t)}{dt} = \frac{i_{L_r}(t)}{C_2} f_2(t) - \frac{i_{L_f}(t)}{C_2} f_2(t), \quad (8)$$

$$\frac{di_{L_f}(t)}{dt} = \frac{v_{C_2}(t)}{L_f} f_2(t) - \frac{v_{C_f}(t)}{L_f} \quad (9)$$

and

$$\frac{dv_{C_f}(t)}{dt} = \frac{i_{L_f}(t)}{C_f} - \frac{v_{C_f}(t)}{R_L C_f}. \quad (10)$$

IV. GENERALIZED AVERAGE DYNAMIC MODEL

The dynamic model is given by the following state equation:

$$\dot{\mathbf{x}}(t) = \mathbf{A}_L \mathbf{x}(t) + \mathbf{B}_L V_{in}, \quad (11)$$

in which, $\mathbf{x}(t) = [y_1, y_2, \dots, y_{n_v}]^T$ is the state vector, \mathbf{A}_L is the state matrix and \mathbf{B}_L the input matrix. y_{n_v} represents a state variable described as: $y_{n_v} = \langle x(t) \rangle_k$, where n_v is the number of state variables. A state variable is evaluated regarding a harmonic k considering the derivative property of Fourier [30]:

$$\frac{d\langle x(t) \rangle_k}{dt} = \langle g(x(t), s_{1,2}) \rangle_k - jk\omega_s \langle x(t) \rangle_k, \quad (12)$$

being $g(x(t), s_{1,2})$ a function that is dependent on a state variable $x(t)$ and a Fourier coefficient $s_{1,2}$. ω_s is the angular operating frequency. In order to achieve a linear model, the switching functions are replaced by the Fourier coefficients. Therefore, the non-linearities from the multiplication of a state variable and a switching function are replaced by terms generated from a convolution operation in the form [30]:

$$\langle x(t) s_{1,2} \rangle_k = \sum_{i=-i_c}^{i_c} \langle x(t) \rangle_{k-i} \langle s_{1,2} \rangle_i, \quad (13)$$

in which, i_c is the convolution index. In practical terms, the convolution operation allows the non-linearities avoidance by generating a sum of products of a state variable by a Fourier switching function coefficient.

Therefore, the differential equations become (time notation t is omitted for simplicity):

$$\frac{d\langle i_{L_c} \rangle_k}{dt} = \frac{V_{in}}{L_c} - \sum_{i=-i_c}^{i_c} \frac{\langle s_1 \rangle_i \langle v_{C_1} \rangle_{k-i}}{L_c} - jk\omega_s \langle i_{L_c} \rangle_k, \quad (14)$$

$$\frac{d\langle v_{C_1} \rangle_k}{dt} = \sum_{i=-i_c}^{i_c} \frac{\langle s_1 \rangle_i \langle i_{L_c} \rangle_{k-i}}{C_1} - \sum_{i=-i_c}^{i_c} \frac{\langle s_1 \rangle_i \langle i_{L_r} \rangle_{k-i}}{C_1} - jk\omega_s \langle v_{C_1} \rangle_k, \quad (15)$$

$$\begin{aligned} \frac{d\langle i_{L_r} \rangle_k}{dt} &= \sum_{i=-i_c}^{i_c} \frac{\langle s_1 \rangle_i \langle v_{C_1} \rangle_{k-i}}{L_r} - \frac{\langle v_{C_r} \rangle_k}{L_r} - \sum_{i=-i_c}^{i_c} \frac{\langle s_2 \rangle_i \langle v_{C_2} \rangle_{k-i}}{L_r} \\ &\quad - jk\omega_s \langle i_{L_r} \rangle_k, \end{aligned} \quad (16)$$

$$\frac{d\langle v_{C_r} \rangle_k}{dt} = \frac{\langle i_{L_r} \rangle_k}{C_r} - jk\omega_s \langle v_{C_r} \rangle_k, \quad (17)$$

$$\frac{d\langle v_{C_2} \rangle_k}{dt} = \sum_{i=-i_c}^{i_c} \frac{\langle s_2 \rangle_i \langle i_{L_r} \rangle_{k-i}}{C_2} - \sum_{i=-i_c}^{i_c} \frac{\langle s_2 \rangle_i \langle i_{L_f} \rangle_{k-i}}{C_2} - jk\omega_s \langle v_{C_2} \rangle_k, \quad (18)$$

$$\frac{d\langle i_{L_f} \rangle_k}{dt} = \sum_{i=-i_c}^{i_c} \frac{\langle s_2 \rangle_i \langle v_{C_2} \rangle_{k-i}}{L_f} - \frac{\langle v_{C_f} \rangle_k}{L_f} - jk\omega_s \langle i_{L_f} \rangle_k, \quad (19)$$

and

$$\frac{d\langle v_{C_f} \rangle_k}{dt} = \frac{\langle i_{L_f} \rangle_k}{C_f} - \frac{\langle v_{C_f} \rangle_k}{R_L C_f} - jk\omega_s \langle v_{C_f} \rangle_k. \quad (20)$$

The set of differential equations should be applied for each value of harmonic k . In addition, the convolution index should be defined in order to solve the summation.

A. LARGE-SIGNAL MODEL

By applying the summations, negative index appear. Also, the sets of differential equations become interdependent. In order to obtain the large-signal model, it is important to note that each state variable with coefficient different from zero has a conjugate that must be considered. In addition, the maximum number of considered harmonics determines the order of the system. For the Class-E² converter, it is necessary to use at least the third-order harmonic component.

The convolution index determines the amount of terms generated by the summations. In this model, it is considered $i_c = 3$. The number of state variables is $n_v = n_o + 2k_{\max}n_o$, being n_o the order of the system. Therefore, the Class-E² converter model has 49 state variables.

Due to the high number of variables, auxiliary variables y are going to be defined in order to represent the real and imaginary parts. The definitions use a index a varying from 1 to k_{\max} with steps of 1 and a index b from 1 to k_{\max} with steps of 2. k must be considered from 0 to k_{\max} with steps of 1. The definitions are shown in Table 3 and they should be applied into the set of differential equations.

In order to explain how the definitions are applied, an example for the choke inductor equation in (14) is going to be presented. By considering $i_c = 3$ and $k_{\max} = 5$ and equating for $k = 0$, the following is obtained:

$$\begin{aligned} \frac{d\langle i_{L_c} \rangle_0}{dt} &= \frac{V_{in}}{L_c} - \frac{\langle s_1 \rangle_{-3} \langle v_{C_1} \rangle_3}{L_c} - \frac{\langle s_1 \rangle_{-2} \langle v_{C_1} \rangle_2}{L_c} \\ &\quad - \frac{\langle s_1 \rangle_{-1} \langle v_{C_1} \rangle_1}{L_c} - \frac{\langle s_1 \rangle_0 \langle v_{C_1} \rangle_0}{L_c} - \frac{\langle s_1 \rangle_1 \langle v_{C_1} \rangle_{-1}}{L_c} \\ &\quad - \frac{\langle s_1 \rangle_2 \langle v_{C_1} \rangle_{-2}}{L_c} - \frac{\langle s_1 \rangle_3 \langle v_{C_1} \rangle_{-3}}{L_c} - j0\omega_s \langle i_{L_c} \rangle_0. \end{aligned} \quad (21)$$

The definitions should be applied into (21):

$$\begin{aligned} \frac{d\langle i_{L_c} \rangle_0}{dt} &= \frac{V_{in}}{L_c} - \frac{\langle s_1 \rangle_{-3} (y_{17} + jy_{18})}{L_c} - \frac{\langle s_1 \rangle_{-2} (y_{15} + jy_{16})}{L_c} \\ &\quad - \frac{\langle s_1 \rangle_{-1} (y_{13} + jy_{14})}{L_c} - \frac{\langle s_1 \rangle_0 y_{12}}{L_c} - \frac{\langle s_1 \rangle_1 (y_{13} - jy_{14})}{L_c} \\ &\quad - \frac{\langle s_1 \rangle_2 (y_{15} - jy_{16})}{L_c} - \frac{\langle s_1 \rangle_3 (y_{17} - jy_{18})}{L_c}. \end{aligned} \quad (22)$$

By evaluating the Fourier coefficients in (2) and replacing in (22), the following is obtained:

Table 3. Definitions for State Variables Considering Harmonic k

Variable	$\langle \cdot \rangle_0$	$\langle \cdot \rangle_{\pm k}$
i_{L_c}	y_1	$y_{2a} \pm jy_{2a+1}$
v_{C_1}	$y_{2k_{\max}+2}$	$y_{2k_{\max}+2+b} \pm jy_{2k_{\max}+3+b}$
i_{L_r}	$y_{4k_{\max}+3}$	$y_{4k_{\max}+3+b} \pm jy_{4k_{\max}+4+b}$
v_{C_r}	$y_{6k_{\max}+4}$	$y_{6k_{\max}+4+b} \pm jy_{6k_{\max}+5+b}$
v_{C_2}	$y_{8k_{\max}+5}$	$y_{8k_{\max}+5+b} \pm jy_{8k_{\max}+6+b}$
i_{L_f}	$y_{10k_{\max}+6}$	$y_{10k_{\max}+6+b} \pm jy_{10k_{\max}+7+b}$
v_{C_f}	$y_{12k_{\max}+7}$	$y_{12k_{\max}+7+b} \pm jy_{12k_{\max}+8+b}$

$$\begin{aligned}
\frac{d\langle i_{L_c} \rangle_0}{dt} &= \frac{V_{in}}{L_c} + \frac{(-1 + D_c)}{L_c} y_{12} \\
&+ \left[\frac{j(1 - \cos(D_c 2\pi) - j\sin(D_c 2\pi))}{2\pi L_c} \quad \frac{j(1 - \cos(D_c 2\pi) + j\sin(D_c 2\pi))}{2\pi L_c} \right] y_{13} \\
&+ \left[\frac{1 - \cos(D_c 2\pi) - j\sin(D_c 2\pi)}{-2\pi L_c} \quad \frac{1 - \cos(D_c 2\pi) + j\sin(D_c 2\pi)}{2\pi L_c} \right] y_{14} \\
&+ \left[\frac{j(1 - \cos(D_c 4\pi) - j\sin(D_c 4\pi))}{4\pi L_c} \quad \frac{j(1 - \cos(D_c 4\pi) + j\sin(D_c 4\pi))}{4\pi L_c} \right] y_{15} \\
&+ \left[\frac{1 - \cos(D_c 4\pi) - j\sin(D_c 4\pi)}{-4\pi L_c} \quad \frac{1 - \cos(D_c 4\pi) + j\sin(D_c 4\pi)}{4\pi L_c} \right] y_{16} \\
&+ \left[\frac{j(1 - \cos(D_c 6\pi) - j\sin(D_c 6\pi))}{6\pi L_c} \quad \frac{j(1 - \cos(D_c 6\pi) + j\sin(D_c 6\pi))}{6\pi L_c} \right] y_{17} \\
&+ \left[\frac{1 - \cos(D_c 6\pi) - j\sin(D_c 6\pi)}{-6\pi L_c} \quad \frac{1 - \cos(D_c 6\pi) + j\sin(D_c 6\pi)}{6\pi L_c} \right] y_{18}.
\end{aligned} \tag{23}$$

The next step is to separate the real and imaginary parts. If the considered harmonic is 0, only the real part should be used. Otherwise, the state variable must be split into two new variables. Rearranging (23) by considering only the real part because $k = 0$, leads to:

$$\begin{aligned}
\frac{dy_1}{dt} &= \frac{V_{in}}{L_c} + \frac{(-1 + D_c)}{L_c} y_{12} + \left(\frac{\sin(D_c 2\pi)}{\pi L_c} \right) y_{13} \\
&+ \left(\frac{-1 + \cos(D_c 2\pi)}{\pi L_c} \right) y_{14} + \left(\frac{\sin(D_c 4\pi)}{2\pi L_c} \right) y_{15} \\
&+ \left(\frac{-1 + \cos(D_c 4\pi)}{2\pi L_c} \right) y_{16} + \left(\frac{\sin(D_c 6\pi)}{3\pi L_c} \right) y_{17} \\
&+ \left(\frac{-1 + \cos(D_c 6\pi)}{3\pi L_c} \right) y_{18}.
\end{aligned} \tag{24}$$

The state variables are now described by the definitions, named by y_{nv} . It can be seen that $d\langle i_{L_c} \rangle_0/dt$ was replaced by dy_1/dt . Equating (14)-(20) for all the state variables is an impractical task. Therefore, it should be solved by software. In this sense, an algorithm is proposed to automatically generated the large-signal state-space model as depicted in the flowchart in Figure 3. It is important to note that, in the construction of the large-signal model, the summations can generate state variables with index higher than k_{max} . In such cases, those terms must be neglected.

The large-signal state space model returns the time response of the auxiliary variables y_{nv} . However, in order to reconstruct the waveforms, it is necessary to invoke the Fourier series by:

$$x(t) = \langle X \rangle_0 + \sum_{k=1}^{k_{max}} 2(\langle X \rangle_k \cos(k\omega_s t) - \langle X \rangle_{-k} \sin(k\omega_s t)), \tag{25}$$

being $\langle X \rangle_0$ the solution of the system in equilibrium considering $k = 0$ given by $\mathbf{X} = -\mathbf{A}^{-1} \cdot \mathbf{B}V_{in}$. The large-signal state-space model is automatically built and it uses symbolic representation. However, its equilibrium solution is

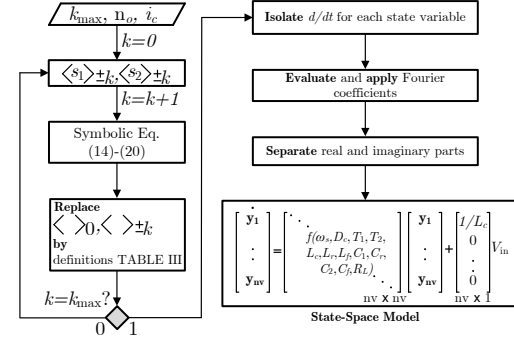


Figure 3. Flowchart for the automatic construction algorithm of the symbolic large-signal model.

numerically solved. In addition $\langle X \rangle_k$ and $\langle X \rangle_{-k}$ represent the solutions for the other harmonics.

The proposed state matrix for the generalized average model of the Class-E² converter is described by Equation (27) in the top of the next page. It is composed by a frequency matrix \mathbf{W}_s , inner state matrices \mathcal{A}_{01} , \mathcal{A}_{02} , \mathcal{A}_1 , \mathcal{A}_2 and \mathcal{A}_3 , and diagonal matrices $\text{diag}(\mathbf{Z})$ and $\text{diag}(\mathbf{RC})$. Terms $\mathbf{0}$ in (27), are 7×7 null matrices. $\text{diag}(\mathbf{Z})$ is based on the term $-1/Z$, in which Z represents a reactive component. $\text{diag}(\mathbf{RC})$ is based on the term $-1/(R_L C_f)$. \mathcal{A}_{01} and \mathcal{A}_{02} relates the DC component variables to the state variables. In addition, input matrix is given as $\mathbf{B}_L = [1/L_c \ 0 \ \dots \ 0]^T$, which has 49 terms. Frequency matrix is given by

$$\mathbf{W}_s = \begin{bmatrix} 0 & 0 & 0 & 0 & 0 & 0 & 0 \\ 0 & 0 & \omega_s & 0 & 0 & 0 & 0 \\ 0 & -\omega_s & 0 & 0 & 0 & 0 & 0 \\ 0 & 0 & 0 & 0 & 2\omega_s & 0 & 0 \\ 0 & 0 & 0 & -2\omega_s & 0 & 0 & 0 \\ 0 & 0 & 0 & 0 & 0 & 0 & 3\omega_s \\ 0 & 0 & 0 & 0 & 0 & -3\omega_s & 0 \end{bmatrix}. \tag{26}$$

Matrices \mathcal{A}_1 , \mathcal{A}_2 and \mathcal{A}_3 relates the AC component variables to the state variables. Figure 4 shows a comparison between circuit simulation and the mathematical results from the large-signal model for the i_{L_r} , v_{C_1} , v_{C_r} and v_{C_2} . The gate signal voltage v_G for the switch S is drawn in Figure 4(a). The agreement between model and simulation shows that the theoretical approach is able to reconstruct the high harmonic content of the Class-E² circuit variables. By setting $k_{max} = 3$, the system has 49 state variables. The small-signal model is similar to the large-signal model. However, the small-signal matrices include the disturbances as shown in the next subsection. The flowchart described in Figure 3 is also used to automatically create the small-signal model.

B. SMALL-SIGNAL MODEL

To evaluate the behaviour of the system under disturbances, the small-signal model is derived from the large-signal model. Perturbations are applied as following:

$$\langle u(t) \rangle_{T_s} = V_{in} + \hat{v}_{in}, \tag{33}$$

$$\mathbf{A}_L = \begin{bmatrix} \mathbf{W}_s & [\mathcal{A}_{01} \ \mathcal{A}_1] & \mathbf{0} & \mathbf{0} & \mathbf{0} & \mathbf{0} & \mathbf{0} \\ [-\mathcal{A}_{01} \ -\mathcal{A}_1] & \mathbf{W}_s & [\mathcal{A}_{01} \ \mathcal{A}_1] & \mathbf{0} & \mathbf{0} & \mathbf{0} & \mathbf{0} \\ \mathbf{0} & [-\mathcal{A}_{01} \ -\mathcal{A}_1] & \mathbf{W}_s & \text{diag}(\mathbf{Z}) & [-\mathcal{A}_{02} \ -\mathcal{A}_2 \ -\mathcal{A}_3] & \mathbf{0} & \mathbf{0} \\ \mathbf{0} & \mathbf{0} & \text{diag}(\mathbf{Z}) & \mathbf{W}_s & \mathbf{0} & \mathbf{0} & \mathbf{0} \\ \mathbf{0} & \mathbf{0} & [\mathcal{A}_{02} \ \mathcal{A}_2 \ \mathcal{A}_3] & \mathbf{0} & \mathbf{W}_s & \mathbf{0} & [-\mathcal{A}_{02} \ -\mathcal{A}_2 \ -\mathcal{A}_3] \\ \mathbf{0} & \mathbf{0} & \mathbf{0} & \mathbf{0} & [\mathcal{A}_{02} \ \mathcal{A}_2 \ \mathcal{A}_3] & \mathbf{W}_s & \text{diag}(\mathbf{Z}) \\ \mathbf{0} & \mathbf{0} & \mathbf{0} & \mathbf{0} & \mathbf{0} & \text{diag}(\mathbf{Z}) & \text{diag}(\mathbf{RC}) + \mathbf{W}_s \end{bmatrix}, \quad (27)$$

$$\mathcal{A}_{01} = \begin{bmatrix} -1+D_c & \frac{\sin(D_c 2\pi)}{2\pi Z} & \frac{-1+\cos(D_c 2\pi)}{2\pi Z} & \frac{\sin(D_c 4\pi)}{4\pi Z} & \frac{-1+\cos(D_c 4\pi)}{4\pi Z} & \frac{D_c 6\pi}{6\pi Z} & \frac{-1+\cos(D_c 6\pi)}{6\pi Z} \end{bmatrix}^T, \quad (28)$$

$$\mathcal{A}_{02} = \begin{bmatrix} \frac{2\pi+T_1-T_2}{2\pi Z} & \frac{\sin(T_1)-\sin(T_2)}{2\pi Z} & \frac{\cos(T_1)-\cos(T_2)}{2\pi Z} & \frac{\sin(2T_1)-\sin(2T_2)}{4\pi Z} & \frac{\cos(2T_1)-\cos(2T_2)}{4\pi Z} & \frac{\sin(3T_1)-\sin(3T_2)}{6\pi Z} & \frac{\cos(3T_1)-\cos(3T_2)}{6\pi Z} \end{bmatrix}^T, \quad (29)$$

$$\mathcal{A}_1 = \begin{bmatrix} \frac{\sin(D_c 2\pi)}{\pi Z} & \frac{-1+\cos(D_c 2\pi)}{\pi Z} & \frac{\sin(D_c 4\pi)}{2\pi Z} & \frac{-1+\cos(D_c 4\pi)}{2\pi Z} & \frac{\sin(D_c 6\pi)}{3\pi Z} & \frac{-1+\cos(D_c 6\pi)}{3\pi Z} \\ \frac{-1+D_c}{Z} + \frac{\sin(D_c 4\pi)}{4\pi Z} & \frac{-1+\cos(D_c 4\pi)}{4\pi Z} & \frac{\sin(D_c 2\pi)}{2\pi Z} + \frac{\sin(D_c 6\pi)}{6\pi Z} & \frac{-4+3\cos(D_c 2\pi)+\cos(D_c 6\pi)}{6\pi Z} & \frac{\sin(D_c 4\pi)}{4\pi Z} & \frac{-1+\cos(D_c 4\pi)}{4\pi Z} \\ \frac{-1+\cos(D_c 4\pi)}{4\pi Z} & \frac{-1+D_c}{Z} - \frac{\sin(D_c 4\pi)}{4\pi Z} & \frac{2-3\cos(D_c 2\pi)+\cos(D_c 6\pi)}{6\pi Z} & \frac{\sin(D_c 2\pi)}{2\pi Z} - \frac{\sin(D_c 6\pi)}{6\pi Z} & \frac{1-\cos(D_c 4\pi)}{4\pi Z} & \frac{\sin(D_c 4\pi)}{4\pi Z} \\ \frac{\sin(D_c 2\pi)}{2\pi Z} + \frac{\sin(D_c 6\pi)}{6\pi Z} & \frac{2-3\cos(D_c 2\pi)+\cos(D_c 6\pi)}{6\pi Z} & \frac{-1+D_c}{Z} & \mathbf{0} & \frac{\sin(D_c 2\pi)}{4\pi Z} & \frac{-1+\cos(D_c 2\pi)}{4\pi Z} \\ \frac{-4+\cos(D_c 2\pi)+\cos(D_c 6\pi)}{6\pi Z} & \frac{\sin(D_c 2\pi)}{2\pi Z} - \frac{\sin(D_c 6\pi)}{6\pi Z} & \frac{-1+D_c}{Z} & \mathbf{0} & \frac{1-\cos(D_c 2\pi)}{2\pi Z} & \frac{\sin(D_c 2\pi)}{2\pi Z} \\ \frac{D_c 4\pi}{4\pi Z} & \frac{1-\cos(D_c 4\pi)}{4\pi Z} & \frac{\sin(D_c 2\pi)}{2\pi Z} & \frac{1-\cos(D_c 2\pi)}{2\pi Z} & \frac{-1+D_c}{Z} & \mathbf{0} \\ \frac{-1+\cos(D_c 4\pi)}{4\pi Z} & \frac{\sin(D_c 4\pi)}{4\pi Z} & \frac{-1+\cos(D_c 2\pi)}{2\pi Z} & \frac{\sin(D_c 2\pi)}{2\pi Z} & \mathbf{0} & \frac{-1+D_c}{Z} \end{bmatrix}, \quad (30)$$

$$\mathcal{A}_2 = \begin{bmatrix} \frac{\sin(T_1)-\sin(T_2)}{\pi Z} & \frac{\cos(T_1)-\cos(T_2)}{\pi Z} & \frac{\sin(2T_1)-\sin(2T_2)}{2\pi Z} \\ \frac{4\pi+2T_1-2T_2+\sin(2T_1)-\sin(2T_2)}{4\pi Z} & \frac{\cos(2T_1)-\cos(2T_2)}{4\pi Z} & \frac{3\sin(T_1)+\sin(3T_1)-3\sin(T_2)-\sin(3T_2)}{6\pi Z} \\ \frac{\cos(2T_1)-\cos(2T_2)}{4\pi Z} & \frac{4\pi+2T_1-2T_2-\sin(2T_1)+\sin(2T_2)}{4\pi Z} & \frac{-3\cos(T_1)+\cos(3T_1)+3\cos(T_2)-\cos(3T_2)}{6\pi Z} \\ \frac{3\sin(T_1)+\sin(3T_1)-3\sin(T_2)-\sin(3T_2)}{6\pi Z} & \frac{-3\cos(T_1)+\cos(3T_1)+3\cos(T_2)-\cos(3T_2)}{6\pi Z} & \frac{2\pi+T_1-T_2}{2\pi Z} \\ \frac{3\cos(T_1)+\cos(3T_1)-3\cos(T_2)-\cos(3T_2)}{6\pi Z} & \frac{3\sin(T_1)-\sin(3T_1)-3\sin(T_2)+\sin(3T_2)}{6\pi Z} & \mathbf{0} \\ \frac{\sin(2T_1)-\sin(2T_2)}{4\pi Z} & \frac{-\cos(2T_1+\cos(2T_2))}{4\pi Z} & \frac{\sin(T_1)-\sin(T_2)}{2\pi Z} \\ \frac{\cos(2T_1)-\cos(2T_2)}{4\pi Z} & \frac{\sin(2T_1)-\sin(2T_2)}{4\pi Z} & \frac{\cos(T_1)-\cos(T_2)}{2\pi Z} \end{bmatrix} \text{ and} \quad (31)$$

$$\mathcal{A}_3 = \begin{bmatrix} \frac{\cos(2T_1)-\cos(2T_2)}{2\pi Z} & \frac{\sin(3T_1)-\sin(3T_2)}{3\pi Z} & \frac{\cos(3T_1)-\cos(3T_2)}{3\pi Z} \\ \frac{3\cos(T_1)+\cos(3T_1)-3\cos(T_2)-\cos(3T_2)}{6\pi Z} & \frac{\sin(2T_1)-\sin(2T_2)}{4\pi Z} & \frac{\cos(2T_1)-\cos(2T_2)}{4\pi Z} \\ \frac{3\sin(T_1)-\sin(3T_1)-3\sin(T_2)+\sin(3T_2)}{6\pi Z} & \frac{-\cos(2T_1)+\cos(2T_2)}{4\pi Z} & \frac{\sin(2T_1)-\sin(2T_2)}{4\pi Z} \\ \mathbf{0} & \frac{\sin(T_1)-\sin(T_2)}{2\pi Z} & \frac{\cos(T_1)-\cos(T_2)}{2\pi Z} \\ \frac{2\pi+T_1-T_2}{2\pi Z} & \frac{-\cos(T_1)-\cos(T_2)}{2\pi Z} & \frac{\sin(T_1)-\sin(T_2)}{2\pi Z} \\ \frac{-\cos(T_1)+\cos(T_2)}{2\pi Z} & \frac{2\pi+T_1-T_2}{2\pi Z} & \mathbf{0} \\ \frac{\sin(T_1)-\sin(T_2)}{2\pi Z} & \mathbf{0} & \frac{2\pi+T_1-T_2}{2\pi Z} \end{bmatrix}. \quad (32)$$

and

$$\langle \omega_s \rangle_{T_s} = \Omega_s + \hat{\omega}_s, \quad (34) \quad \langle y(t) \rangle_{T_s} = Y + \hat{y}, \quad (35)$$

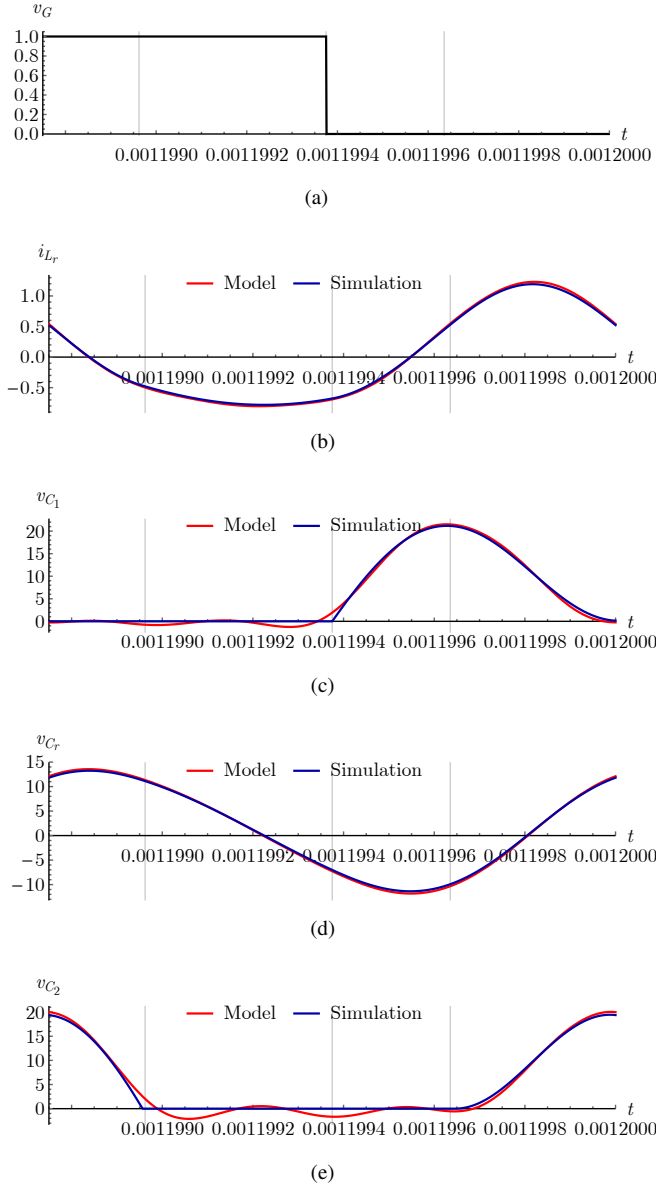


Figure 4. Comparison between large-signal model and simulation. (a) Gate signal voltage v_G . (b) Resonant inductor current i_{L_r} . (c) Inverter capacitor voltage v_{C_1} . (d) Resonant capacitor voltage v_{C_r} . (e) Rectifier capacitor voltage v_{C_2} .

in which: \hat{v}_{in} , $\hat{\omega}_s$ and \hat{y} are small variations in the input source, frequency and state variables, respectively. Ω_s is the operating frequency and Y is the equilibrium solution of the large-signal model, which means $Y = X$. In this sense, the small-signal solution is only possible if the large-signal model was previously obtained. The small-signal model is represented by its state-space representation

$$\dot{\hat{x}}(t) = \mathbf{A}_S \hat{x}(t) + \mathbf{B}_S \hat{u}_d(t). \quad (36)$$

The state-vector of the small-signal model is given as

$$\hat{x}(t) = [\hat{y}_1, \hat{y}_2, \hat{y}_3, \dots, \hat{y}_{nv}]^T. \quad (37)$$

$\hat{u}_d(t)_{2 \times 1}$ represents the disturbances that can be added to evaluate the model. In this case, frequency and input source are considered, thus

$$\hat{u}_d(t)_{2 \times 1} = \begin{bmatrix} \hat{\omega}_s \\ \hat{v}_{in} \end{bmatrix}. \quad (38)$$

The state-space matrices are based on the differential equations after the perturbation and linearization. The small-signal differential equations for the Class-E² resonant converter are given by

$$\frac{d\langle \hat{i}_{L_c} \rangle_k}{dt} = \frac{\hat{v}_{in}}{L_c} \sum_{i=-i_c}^{i_c} \langle s_1 \rangle_i \langle v_{\hat{C}_1} \rangle_{k-i} - jk\Omega_s \langle \hat{i}_{L_c} \rangle_k - jk\hat{\omega}_s \langle I_{L_c} \rangle_k, \quad (39)$$

$$\begin{aligned} \frac{d\langle v_{\hat{C}_1} \rangle_k}{dt} &= \sum_{i=-i_c}^{i_c} \langle s_1 \rangle_i \langle \hat{i}_{L_c} \rangle_{k-i} - \sum_{i=-i_c}^{i_c} \langle s_1 \rangle_i \langle \hat{i}_{L_r} \rangle_{k-i} - jk\Omega_s \langle v_{\hat{C}_1} \rangle_k \\ &\quad - jk\hat{\omega}_s \langle V_{C_1} \rangle_k, \end{aligned} \quad (40)$$

$$\begin{aligned} \frac{d\langle \hat{i}_{L_r} \rangle_k}{dt} &= \sum_{i=-i_c}^{i_c} \langle s_1 \rangle_i \langle v_{\hat{C}_1} \rangle_{k-i} - \frac{\langle v_{\hat{C}_r} \rangle_k}{L_r} - \sum_{i=-i_c}^{i_c} \langle s_2 \rangle_i \langle v_{\hat{C}_2} \rangle_{k-i} \\ &\quad - jk\Omega_s \langle \hat{i}_{L_r} \rangle_k - jk\hat{\omega}_s \langle I_{L_r} \rangle_k, \end{aligned} \quad (41)$$

$$\frac{d\langle v_{\hat{C}_r} \rangle_k}{dt} = \frac{\langle \hat{i}_{L_r} \rangle_k}{C_r} - jk\Omega_s \langle v_{\hat{C}_r} \rangle_k - jk\hat{\omega}_s \langle V_{C_r} \rangle_k, \quad (42)$$

$$\begin{aligned} \frac{d\langle v_{\hat{C}_2} \rangle_k}{dt} &= \sum_{i=-i_c}^{i_c} \langle s_2 \rangle_i \langle \hat{i}_{L_r} \rangle_{k-i} - \sum_{i=-i_c}^{i_c} \langle s_2 \rangle_i \langle \hat{i}_{L_f} \rangle_{k-i} - jk\Omega_s \langle v_{\hat{C}_2} \rangle_k \\ &\quad - jk\hat{\omega}_s \langle V_{C_2} \rangle_k, \end{aligned} \quad (43)$$

$$\begin{aligned} \frac{d\langle \hat{i}_{L_f} \rangle_k}{dt} &= \sum_{i=-i_c}^{i_c} \langle s_2 \rangle_i \langle v_{\hat{C}_2} \rangle_{k-i} - \frac{\langle v_{\hat{C}_f} \rangle_k}{L_f} - jk\Omega_s \langle \hat{i}_{L_f} \rangle_k \\ &\quad - jk\hat{\omega}_s \langle I_{L_f} \rangle_k, \end{aligned} \quad (44)$$

and

$$\frac{d\langle v_{\hat{C}_f} \rangle_k}{dt} = \frac{\langle \hat{i}_{L_f} \rangle_k}{C_f} - \frac{\langle v_{\hat{C}_f} \rangle_k}{R_L C_f} - jk\Omega_s \langle v_{\hat{C}_f} \rangle_k - jk\hat{\omega}_s \langle V_{C_f} \rangle_k. \quad (45)$$

In the same way of the large-signal model, (39)-(45) should be evaluated considering $\mathbf{k} = [0 \dots \mathbf{k}_{\max}]$. The dynamic matrix is similar to the one developed for the large-signal model. The difference is related to the term Ω_s , which replaces ω_s .

V. RESULTS

A Class-E² resonant converter was designed and assembled in a printed circuit board in order to experimentally verify the theoretical approach. Aiming to test the frequency disturbance, it is necessary to include a gate-driver circuit for the switch S based on voltage-controlled oscillator (VCO). For this purpose, the high speed logic phase-locked-loop with VCO [31] was selected.

The VCO provides the input signal for the switch gate-driver, which ensures the proper gate voltage to the MOSFET. Both VCO and switch gate-driver are supplied by the main input source. Notwithstanding, an auxiliary voltage source can be used to perform a step voltage signal in the VCO, which results in a frequency disturbance. The hardware components are detailed in Table 4. The designed converter is shown in Figure 5.

In order to verify the large-signal model, the waveforms were measured considering the steady-state operation. The inverter capacitor voltage v_{C_1} and the rectifier capacitor voltage v_{C_2} are shown in Figure 6 and Figure 7, respectively, by considering a comparison between model and experimental. These circuit variables were selected because they dictate the soft-switching operation of the converter, thereupon, they can be used as a proof-of-concept. In addition, the results for the resonant capacitor voltage v_{C_r} are shown in Figure 8.

The capacitor C_1 and C_2 voltages are slightly higher in the model. In this sense, it should be noted that, the model does not consider the VCO circuit, which is also powered up by the main input source. In addition, ideal components are considered in the model, which leads to the aforementioned differences between theory and experimental.

In the interest of validate the small-signal model, a disturbance was applied in the operating frequency. By applying a voltage step in the VCO, the gate-driver signal frequency is changed. Figure 9 depicts the result considering a frequency disturbance of 28 kHz.

The stabilization time after the disturbance is approximate 1 ms, which is confirmed by measurement. During the transient time, 1.7 V of ΔV is predicted by the model, while 1.5 V was measured. Nonetheless, for both large-signal and small-signal models, the experimental results are in agreement with theory.

In order to highlight the advantage of the generalized averaged model over the standard averaged model, a comparison is shown in Figure 10. Both methods were implemented in a step-down Buck converter in continuous conduction mode. This topology is used because it is commonly modeled by the averaged model. However, if the waveform oscillations are increased, the averaged model is not suitable. The oscillations can be evaluated by the low-pass LC filter frequency normalized by the switching frequency, f_o/f_s , where $f_o = 1/2\pi\sqrt{LC}$. Figure 10 shows that, higher f_o/f_s , higher is the output voltage V_o ripple. The standard averaged model is suitable for low values of f_o/f_s . In Figure 10(c)

Table 4. Hardware Components

Component	Value	Part number
Choke inductor, L_c	470 μ H	CDRH127
Inverter capacitor, C_1	8.2 nF	1206B822K500CT
Resonant inductor, L_r	5.2 μ H	CDRH104RNP-5R2NC
Resonant capacitor, C_r	12 nF	0805B123K500NT
Rectifier capacitor, C_2	6.8 nF	0402B682K500NT
Output inductor, L_f	150 μ H(3)	CKCS8040-150uH/M
Output inductor, L_f	30 μ H	FNR6045S300MT
Output capacitor, C_f	8.2 nF	1206B822K500CT
Inverter switch, S	-	FDS6690A
Rectifier diode, D	-	PDS5100-13
VCO, U_1	-	CD74HC4046AE
VCO capacitor, C_{VCO}	120 pF	CC4-0805-CG
VCO resistor, R_{VCO}	3.3 k Ω	0805W8F3301T5E
Voltage divider resistor, R_{DIV1}	4.7 k Ω	0603WAF4701T5E
Voltage divider resistor, R_{DIV2}	24 k Ω	0603WAF2402T5E
Switch gate-driver, U_2	-	UCC27519DBVR
Gate-driver capacitor, C_G	1 μ H	CL31B105KBHNNNE
Gate-driver resistor, R_G	2 Ω	0805W8F200KT5E
Nominal input voltage, V_{in}	6 V	
Operating frequency, f_s	800 kHz	

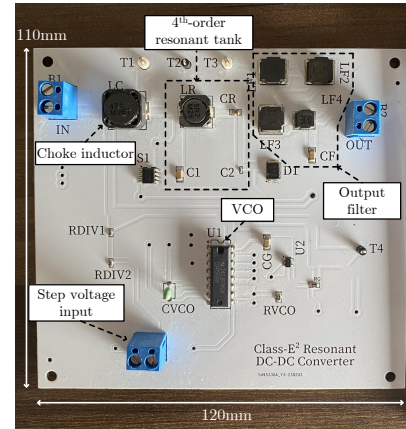


Figure 5. Designed Class-E² DC-DC resonant converter based on VCO.

and Figure 10(d), it can be seen that, it is necessary to use the GAM in order to reconstruct the waveform.

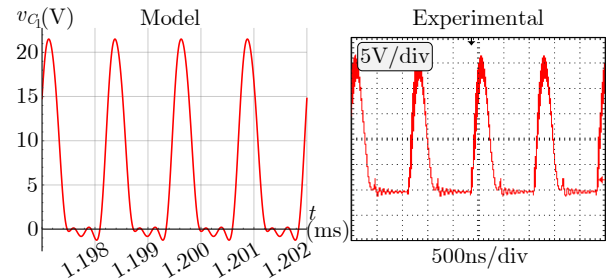


Figure 6. Large-signal model validation. (a) Inverter capacitor voltage model. (b) Inverter capacitor voltage measurement.

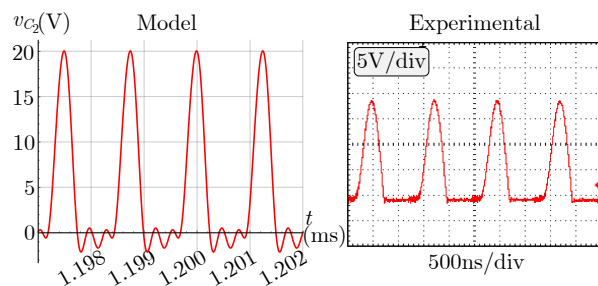


Figure 7. Large-signal model validation. (a) Rectifier capacitor voltage model. (b) Rectifier capacitor voltage measurement.

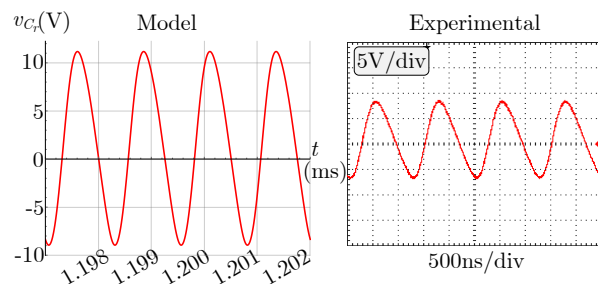


Figure 8. Large-signal model validation. (a) Resonant capacitor voltage model. (b) Resonant capacitor voltage measurement.

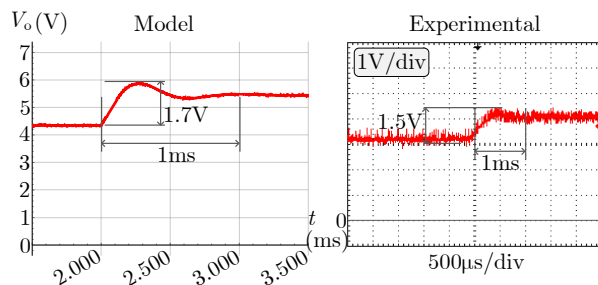
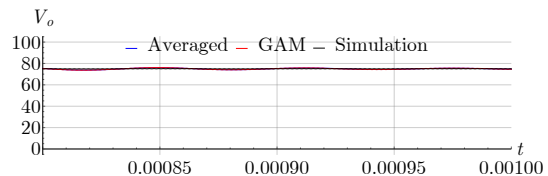


Figure 9. Small-signal model validation considering a 28 kHz frequency disturbance. (a) Output voltage model. (b) Output voltage measurement.

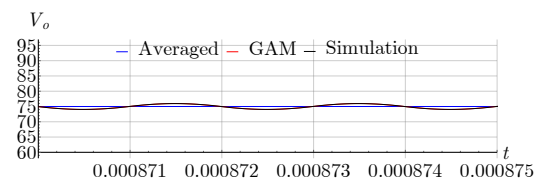
VI. CONCLUSION

In this work, the generalized average model of the Class- E^2 DC-DC resonant converter has been proposed. The main contribution concerning the state-of-art in dynamic model techniques for power converters is that the presented work is able to built the large-signal and small-signal models by considering high-order harmonics. Particularly, the interface voltage between inverter and rectifier sides (rectifier diode voltage), which requires at least the third-order harmonic.

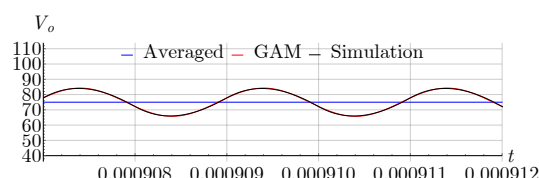
Furthermore, a systematic way to deal with the negative index generate by the convolution and the real and imaginary parts due to the Fourier coefficients has been addressed. The generalized differential large-signal and small-signal equations for the Class- E^2 converter and how to represent it in an usable state-space model have been presented. In order to verify the theory, a Class- E^2 converter was assembled



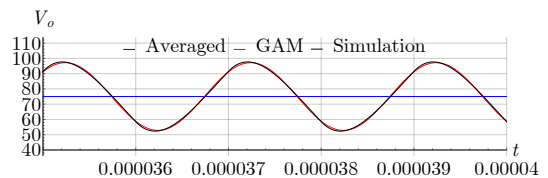
(a)



(b)



(c)



(d)

Figure 10. Comparison among averaged model, GAM and simulation. (a) $\frac{f_o}{f_s} = 0.03$. (b) $\frac{f_o}{f_s} = 0.1$. (c) $\frac{f_o}{f_s} = 0.3$. (d) $\frac{f_o}{f_s} = 0.5$.

and it uses a VCO to perform the frequency disturbance. The large-signal model was confirmed by measuring the inverter capacitor and rectifier diode voltages, which dictates the ZVS and ZDVS conditions, respectively. In addition, the resonant capacitor voltage was verified. The small-signal model was validated by applying a frequency disturbance and comparing the model and experimental output voltages. The matching between theory and experimental validates the model and it can be used to evaluate the dynamic behavior Class- E^2 DC-DC resonant converters; therefore, improving new-flanged technologies in wireless power transfer system, battery charger and electric vehicle applications.

AUTHOR'S CONTRIBUTIONS

Conceptualization, Data Curation, Formal Analysis, Investigation, Methodology, Software, Validation, Writing – Original Draft, Writing – Review & Editing: MENDONÇA, L.S.; Conceptualization, Formal Analysis, Investigation, Methodology, Project Administration, Resources, Software, Supervision, Writing – Original Draft: BISOGNO, F.E.

PLAGIARISM POLICY

This article was submitted to the similarity system provided by Crossref and powered by iThenticate—Similarity Check.

References

- [1] Z. Shu, Y. Fengfa, W. Yijie, J. M. Alonso, “A 500-kHz ZVS Class-E Type DC–DC Converter With Two Anti-Series mosfets Topology”, *IEEE Transactions on Power Electronics*, vol. 38, no. 9, pp. 10810–10820, September 2020, doi:10.1109/TPEL.2023.3287161.
- [2] T. Nagashima, X. Wei, E. Bou, E. Alarcón, M. K. Kazimierczuk, H. Sekiya, “Analysis and Design of Loosely Inductive Coupled Wireless Power Transfer System Based on Class-E² DC-DC Converter for Efficiency Enhancement”, *IEEE Transactions on Circuits and Systems I: Regular Papers*, vol. 62, no. 11, pp. 2781–2791, November 2015, doi:10.1109/TCSI.2015.2482338.
- [3] R. D. Middlebrook, S. Cuk, “A General Unified Approach to Modelling Switching-Converter Power Stages”, in *1976 IEEE Power Electronics Specialists Conference*, pp. 18–34, 1976, doi:10.1109/PESC.1976.7072895.
- [4] E. V. Dijk, J. N. Spruijt, D. M. O’Sullivan, J. B. Klaassens, “PWM-Switch Modeling of DC-DC Converters”, *IEEE Transactions on Power Electronics*, vol. 10, no. 6, pp. 659–665, November 1995, doi:10.1109/63.471285.
- [5] J. A. da Rocha Carvalho, F. L. Tofoli, “Small-Signal Model Validation of a SEPIC Converter based on the Three-State Switching Cell in CCM using the PWM Switch Model”, in *2017 Brazilian Power Electronics Conference (COBEP)*, pp. 1–6, 2017, doi:10.1109/COBEP.2017.8257220.
- [6] M. C. N. E. Niculescu, D. M. Purcaru, “Modelling the PWM Zeta converter in Discontinuous Conduction Mode”, in *MELECON 2008 - The 14th IEEE Mediterranean Electrotechnical Conference*, pp. 651–657, 2008, doi:10.1109/MELCON.2008.4618509.
- [7] E. Vuthchhay, C. Bunlaksanusorn, H. Hirata, “Dynamic Modeling and Control of a Zeta Converter”, in *2008 International Symposium on Communications and Information Technologies*, pp. 498–503, 2008, doi:10.1109/ISCIT.2008.4700242.
- [8] P. Wang, X. Chen, C. Tong, P. Jia, C. Wen, “Large- and Small-Signal Average-Value Modeling of Dual-Active-Bridge DC–DC Converter With Triple-Phase-Shift Control”, *IEEE Transactions on Power Electronics*, vol. 36, no. 8, pp. 9237–9250, August 2021, doi:10.1109/TPEL.2021.3052459.
- [9] X. W. X. Yue, F. Blaabjerg, “Review of Small-Signal Modeling Methods Including Frequency-Coupling Dynamics of Power Converters”, *IEEE Transactions on Power Electronics*, vol. 34, no. 4, pp. 3313–3328, April 2019, doi:10.1109/TPEL.2018.2848980.
- [10] Y.-D. Choi, D.-Y. Lee, D.-S. Hyun, “A Study on the New Control Scheme of Class-E inverter for IH-jar Application with Clamped Voltage Characteristics using Pulse Frequency Modulation”, in *Conference Record of the 2002 IEEE Industry Applications Conference*, pp. 1346–1351, 2002, doi:10.1109/IAS.2002.1042732.
- [11] S. H. L. Tu, H.-W. Yeh, “A PWM Controller with Table Look-up for DC-DC Class E Buck/Boost Conversion”, in *2013 IEEE International Conference of Electron Devices and Solid-state Circuits*, pp. 1–2, 2013, doi:10.1109/EDSSC.2013.6628039.
- [12] Y. Li, X. Ruan, “Output Current Limitation for ON–OFF Controlled Very-High-Frequency Class E DC–DC Converter”, *IEEE Transactions on Industrial Electronics*, vol. 69, no. 11, pp. 11826–11831, November 2022, doi:10.1109/TIE.2021.3116594.
- [13] A. Celentano, F. Pareschi, R. Rovatti, G. Setti, “A Zero-Transient Dual-Frequency Control for Class-E Resonant DC–DC Converters”, *IEEE Transactions on Power Electronics*, vol. 38, no. 2, pp. 2105–2114, February 2023, doi:10.1109/TPEL.2022.3208816.
- [14] Y. Li, X. Ruan, L. Zhang, Y. K. Lo, “Multipower-Level Hysteresis Control for the Class E DC–DC Converters”, *IEEE Transactions on Power Electronics*, vol. 35, no. 5, pp. 5279–5289, May 2020, doi:10.1109/TPEL.2019.2940043.
- [15] N. J. Dahl, A. M. Ammar, A. Knott, M. A. E. Andersen, “An Improved Linear Model for High-Frequency Class-DE Resonant Converter Using the Generalized Averaging Modeling Technique”, *IEEE Journal of Emerging and Selected Topics in Power Electronics*, vol. 8, no. 3, pp. 2156–2166, September 2020, doi:10.1109/JESTPE.2019.2945182.
- [16] R. Engleitner, F. E. Bisogno, J. R. Pinheiro, C. Rech, L. Michels, M. Radecker, “Small-Signal Modeling of a DC-DC Class-E Piezo-converter based on Generalized Averaging Method”, in *2011 IEEE International Symposium on Industrial Electronics*, 2011, doi:10.1109/ISIE.2011.5984191.
- [17] E. X.-Q. Yangi, *Extended Describing Function Method for Small-Signal of Resonant and Multi-Resonant Converters*, Ph.D. thesis, Faculty of the Virginia Polytechnic Institute and State University, Blacksburg, Virginia, 1994.
- [18] C. H. Chang, E. C. Chang, C. A. Cheng, H. L. Cheng, S. C. Lin, “Small Signal Modeling of LLC Resonant Converters Based on Extended Describing Function”, in *2012 International Symposium on Computer, Consumer and Control*, pp. 365–368, 2012, doi:10.1109/IS3C.2012.99.
- [19] P. Azer, A. Emadi, “Generalized State Space Average Model for Multi-Phase Interleaved Buck, Boost and Buck-Boost DC-DC Converters: Transient, Steady-State and Switching Dynamics”, *IEEE Access*, vol. 8, pp. 77735–77745, 2020, doi:10.1109/ACCESS.2020.2987277.
- [20] A. Ayachit, M. K. Kazimierczuk, “Averaged Small-Signal Model of PWM DC-DC Converters in CCM Including Switching Power Loss”, *IEEE Transactions on Circuits and Systems II: Express Briefs*, vol. 66, no. 2, pp. 262–266, February 2019, doi:10.1109/TCSII.2018.2848623.
- [21] F. J. Nogueira, L. J. G. Resende, R. M. Ferraz, F. O. Coelho, E. S. Silva, G. M. Soares, H. A. C. Braga, “Modelagem e Controle de um Driver de LEDs de Baixa Frequência baseado no Pré-Regulador Boost”, *Eletrônica de Potência*, vol. 22, no. 4, pp. 350–361, Dezembro 2017, doi:10.18618/REP.2017.4.2699.
- [22] Y. Zhang, S. Buso, “Generalized Average Modeling of Bidirectional Interleaved Boost with Coupled Inductors Converter”, in *2021 23rd European Conference on Power Electronics and Applications (EPE’21 ECCE Europe)*, pp. 1–9, 2021, doi:10.23919/EPE21ECCEEurope50061.2021.9570618.
- [23] V. Vorperian, R. Tymerski, F. C. Y. Lee, “Equivalent Circuit Models for Resonant and PWM Switches”, *IEEE Transactions on Power Electronics*, vol. 4, no. 2, pp. 205–214, April 1989, doi:10.1109/63.24905.
- [24] J. A. Mueller, J. W. Kimball, “An Improved Generalized Average Model of DC–DC Dual Active Bridge Converters”, *IEEE Transactions on Power Electronics*, vol. 33, no. 11, pp. 9975–9988, November 2018, doi:10.1109/TPEL.2018.2797966.
- [25] P. F. S. Costa, P. H. B. Löbler, A. Toebe, L. Roggia, L. Schuch, “Modelagem e Controle do Conversor DAB Aplicado à Carga de Baterias”, *Eletrônica de Potência*, vol. 23, no. 3, pp. 292–301, Setembro 2018, doi:10.18618/REP.2018.3.2780.
- [26] M. F. Menke, A. R. Seidel, R. V. Tambara, “LLC LED Driver Small-Signal Modeling and Digital Control Design for Active Ripple Compensation”, *IEEE Transactions on Industrial Electronics*, vol. 66, no. 1, pp. 387–396, January 2019, doi:10.1109/TIE.2018.2829683.
- [27] W. J. Gu, K. Harada, “A Circuit Model for the Class E Resonant DC-DC Converter Regulated at a Fixed Switching Frequency”, *IEEE Transactions on Power Electronics*, vol. 7, no. 1, pp. 99–110, January 1992, doi:10.1109/63.124582.
- [28] W. Zhu, H. Sekiya, “A 1MHz Class-E2 Single-Stage PFC Converter with Frequency Control”, in *2020 IEEE Applied Power Electronics Conference and Exposition (APEC)*, pp. 2041–2047, 2020, doi:10.1109/APEC39645.2020.9124248.
- [29] L. S. Mendonça, J. P. S. Cipriani, T. C. Naidon, F. E. Bisogno, “Steady-State Analysis and Design Methodology for Class-E2 Resonant DC/DC Converters based on a Normalized State-Space Model”, *Eletrônica de Potência*, vol. 25, no. 2, pp. 209–218, Junho 2020, doi:10.18618/REP.2020.2.0002.
- [30] S. R. Sanders, J. M. Noworolski, X. Z. Liu, G. C. Verghesal, “Generalized Averaging Method for Power Conversion Circuits”, *IEEE Transactions on Power Electronics*, vol. 6, no. 2, pp. 251–259, April 1991, doi:10.1109/63.76811.
- [31] Texas Instruments, “High-speed CMOS logic phase-locked loop with VCO, CD74HC4046A datasheet”, [Online], 2003.

BIOGRAPHIES

Lucas Sangoi Mendonça is a control and automation engineer (2015), master (2017) and doctor in Electrical Engineering (2021) with the Federal University of Santa Maria. He is currently a professor at Federal University

of Technology-Paraná. His areas of interest are: resonant and pwm dc-dc converters, ac-dc resonant rectifiers and dc-ac resonant inverters.

Fábio Ecke Bisogno is an electrical engineer (1999), master (2001) in Electrical Engineering with the Federal University of Santa Maria, and

doctor in Electrical Engineering with the Technische Universität Chemnitz (2006). He is currently a professor at Hochschule Koblenz. His areas of interest are: resonant converters, self-oscillating electronic converters and artificial lighting.